

Anomalous thermal expansion in a CuAl₂-type superconductor CoZr₂

Yoshikazu Mizuguchi^{1*}, Md. Riad Kasem¹, Yoichi Ikeda²

¹*Department of Physics, Tokyo Metropolitan University, Hachioji, Tokyo 192-0397, Japan.*

²*Institute for Materials Research, Tohoku University, Sendai, Miyagi 987-6543, Japan*

E-mail: mizugu@tmu.ac.jp

We performed neutron powder diffraction and X-ray powder diffraction on a CuAl₂-type superconductor CoZr₂ and observed remarkably anisotropic thermal expansion in a wide temperature range of $T = 50\text{--}573$ K. With decreasing temperature, the lattice constant a decreases, while the lattice constant c continuously increases in CoZr₂. The origin of the anisotropic shrinkage/expansion of the a -axis/ c -axis by cooling is explained by the small change in the Co-Zr bond and the systematic decrease in the Zr-Co-Zr angle. Similar thermal expansion was observed in alloyed systems, (Fe,Co,Ni)Zr₂ and (Fe,Co,Ni,Rh,Ir)Zr₂, which suggests that the phenomenon is common feature in the $TrZr_2$ system.

Materials that exhibit negative thermal expansion (NTE) or zero thermal expansion (ZTE) have been developed in a wide range of materials because that can be used for various applications including the use in precision instruments.¹⁻⁵⁾ The typical NTE material is ZrW_2O_8 , which exhibits a large isotropic NTE over a wide range of temperatures (T).⁴⁾ In ZrW_2O_8 , the origin of the NTE is its characteristic flexible network on the atomic bonding and linkage of the units. In addition, NTE has been observed in various compounds that exhibit a phase transition. The driving force includes a metal-insulator transition,^{5,6)} magnetovolume effects,^{7,8)} intermetallic charge transfer,^{9,10)} valence crossover (or transition),^{11,12)} and ferroelectric transition.^{13,14)} Furthermore, NTE has been observed in various superconductors or related antiferromagnetic phases.¹⁵⁻²¹⁾ In most cases of NTE in superconductors, the origin of the NTE is linked to the emergence of the superconducting order parameter; hence, the NTE is typically observed below the transition temperature (T_c).³⁾ In addition, there are superconductors that exhibit NTE at temperatures well above its T_c : the typical example is the BSCCO superconductor.¹⁷⁾ Since the thermal expansion characteristics of superconductors is critical when fabricating superconducting wires or films, studies on thermal expansion on superconductors have been performed in a wide temperature range so far.²²⁻²⁴⁾

Here, we show anomalously anisotropic thermal expansion in CoZr_2 and alloyed TrZr_2 (Tr: Fe, Co, Ni, Rh, Ir). We observed contrasting thermal expansions of the a -axis and the c -axis in the tetragonal unit cell. In the wide temperature range of $T = 50\text{--}572$ K ($T = 572$ K is the highest temperature examined in this study), CoZr_2 exhibits continuous positive thermal expansion (PTE) of the a -axis and NTE of the c -axis. As a result of the contrasting expansions, the lattice volume does not remarkably decrease by the decrease in temperature.

Figure 1 shows the schematic images of the crystal structure of CoZr_2 with a CuAl_2 -type tetragonal structure (space group #140). The framework is composed of the CoZr_8 polyhedron units, which are stacked along the c -axis. T_c of TrZr_2 with $\text{Tr} = \text{Ni, Co, Rh, Ir}$ is 3.2, 5.2, 11.3, and 7.5 K, respectively.²⁵⁾ The electronic density of states (DOS) near the Fermi energy (E_F) is mainly composed of the hybridization of Zr- d and Co- d orbitals.²⁶⁾ Noticeably, the T_c of CoZr_2 increases with application of external pressures: $T_c = 9.5$ K at 8 GPa.²⁶⁾ The huge pressure effect implies the flexible crystal structure, which would largely modify the electronic DOS and/or electron-phonon coupling in the system under high pressures. In addition, we recently developed alloyed compounds of TrZr_2 by drawing the high-entropy-alloy (HEA) concept.²⁷⁻²⁹⁾ Interestingly, the T_c of TrZr_2 increases with increasing lattice constant c , while the variation of the element, the concentration,

configurational entropy of mixing at the *Tr* site do not have an impact on T_c though the strong disorder was introduced by alloying on the *Tr* site. This trend also implies the importance of chemical bonds along the *c*-axis in the *Tr*Zr₂ superconductors. Motivated by those backgrounds on the relationship between superconductivity and the crystal structure in *Tr*Zr₂, we decided to perform crystal structure analyses for CoZr₂ and the alloyed compounds in a wide temperature range.

The polycrystalline samples of CoZr₂, Fe_{1/3}Co_{1/3}Ni_{1/3}Zr₂ (abbreviated as (Fe,Co,Ni)Zr₂), and Fe_{0.2}Co_{0.2}Ni_{0.2}Rh_{0.2}Ir_{0.2}Zr₂ (abbreviated as (Fe,Co,Ni,Rh,Ir)Zr₂) were prepared by arc melting using powders of Fe (99.9%), Co (99%), Ni (99.9%), Rh (99.9%) and Ir (99.9%) and plates of Zr (99.2%) as described in Ref. 29. The phase purity and the crystal structure were examined by X-ray powder diffraction (XRD) with Cu-K α radiation by the θ -2 θ method on Miniflex-600 (RIGAKU) equipped with a high-resolution semiconductor detector D/tex-Ultra. For high-temperature XRD on Miniflex-600, the sample temperature was controlled by the BTS500 attachment. For low-temperature experiments, we performed neutron powder diffraction (NPD) with a HERMES diffractometer³⁰⁾ installed at the T1-3 guide port in the JRR-3 of the Japan Atomic Energy Agency, Tokai. A thermal neutron beam was monochromatized to be 2.197(1) Å with a vertically-focused Ge (331) monochromator. Typical instrumental parameters were determined by analyzing line positions and line shapes of a standard reference material (LaB₆, NIST660c).³¹⁾ Powder samples were sealed in a vanadium cylinder cell with ϕ 6 mm-diameter (thickness 0.1 mm) and ~60mm-length in a ⁴He gas atmosphere. A closed-cycle refrigerator was used to cool the samples and controlled from a base temperature ($T < 10$ K) to room temperature. The obtained XRD and NPD patterns were refined by the Rietveld method using RIETAN-FP,³²⁾ and the schematic images of the refined crystal structure were depicted using VESTA.³³⁾ T_c of the samples were confirmed by magnetization measurements by a superconducting interference device (SQUID) with an applied field of 10 Oe on MPMS3 (Quantum Design), and the magnetization data are shown in Supplementary data (Fig. S1). All the examined samples showed bulk superconductivity with a large diamagnetic signal, and the evaluated T_c for CoZr₂, (Fe,Co,Ni)Zr₂, and (Fe,Co,Ni,Rh,Ir)Zr₂ is 6.0, 3.3, and 5.4 K, respectively.

Figure 2(a) shows the NPD patterns for CoZr₂ taken at $T = 50, 100, 170$, and 293 K (room temperature). The profiles at $T = 50$ and 293 K are similar, and no crystal structural transition and magnetic ordering were observed. As displayed in Fig. 2(b), we observed a decrease in the lattice constant a (from the 200 peak) and an increase in the lattice constant

c (from the 002 peak). To obtain the temperature dependences of lattice constants, the NPD patterns were analyzed by Rietveld method with a three-phase mode as shown in Fig. 2(c) and Fig. S2 (supplementary data); the refined structural parameters are summarized in Table I. Here, we identified the two impurity phases of CoZr_3 (16%, space group #63) and CoZr (5%, space group #225). Figures 2(d–f) show the temperature dependences of lattice constants a , c , and V for CoZr_2 . With decreasing temperature, the lattice constant a decreases, which is PTE, and the lattice constant c increases, which is NTE. The high-temperature XRD results also exhibit the same trend (see supplementary data for the XRD patterns). Since the a -axis and the c -axis exhibit contrasting PTE/NTE, the lattice volume (V) does not show monotonous changes.

To understand the origin of the anomalous (or anisotropic) thermal expansion of the a -axis and the c -axis, the atomic distances of Co-Zr, Co-Co, and Zr-Zr are evaluated from NPD and XRD data and summarized in Table I (See Fig. 1 for the labels of the distances and the angle). The Co-Co (i) distance is directly linked to the lattice constant c , and it increases with decreasing temperature. The Co-Co (ii) and Zr-Zr (ii) distances decrease with decreasing temperature, which can be understood with the a -axis compression. We found that the Co-Zr and Zr-Zr (i) distances do not largely change at low temperatures. Since the Zr-Zr (i) distance is relatively larger than that of the other bonds, and the Co-Zr bond should be essential for this compound, we consider that the origin of the c -axis expansion is linked to the bonding character of the Co-Zr bond. As a fact, Zr-Co-Zr angle shows systematic decrease with decreasing temperature. Therefore, we conclude that the anomalous anisotropic thermal expansion (elongation of the unit cell) in CoZr_2 is induced by the robust Co-Zr distance to the temperature change and the flexible Zr-Co-Zr angle in the CoZr_8 polyhedron.

In this study, we examined low-temperature crystal structures for the alloyed compounds, $(\text{Fe,Co,Ni})\text{Zr}_2$ and $(\text{Fe,Co,Ni,Rh,Ir})\text{Zr}_2$ as well. For $(\text{Fe,Co,Ni})\text{Zr}_2$, three-phase analysis same as the case of CoZr_2 was performed. For, $(\text{Fe,Co,Ni,Rh,Ir})\text{Zr}_2$, due to the presence of unknown impurity peaks, we performed single-phase analysis. See supplementary data for the Rietveld refinement results for those samples. In Figs. 3(a–f), the temperature dependences of lattice constants a , c , and V for those alloyed samples are shown. Noticeably, the contrasting thermal expansion, PTE of the a -axis and NTE of the c -axis, was observed for both $(\text{Fe,Co,Ni})\text{Zr}_2$ and $(\text{Fe,Co,Ni,Rh,Ir})\text{Zr}_2$. In addition, the trend on the temperature evolution of the TrZr_8 polyhedron is similar; namely, the change in Tr-Zr distance is small and the Zr-Tr-Zr angle systematically decreases with decreasing

temperature (see Tables in supplementary data for the refined parameters).

Here, we briefly discuss about the origin of the anomalous (contrasting anisotropic) thermal expansion in $TrZr_2$. According to the binary Co-Zr phase diagram, the $CuAl_2$ -type $CoZr_2$ phase is congruent melting, and no structural transition is expected at temperatures higher than 572 K. In addition, no magnetic ordering was observed in our NPD results. Furthermore, the NTE of the c -axis occurs at temperatures well above T_c of 6.0 K in $CoZr_2$. Although we have to confirm the possibility of the change in valence state of Tr (i.e. electronic and bonding states of Tr) to exclude the possibility of valence-state-driven NTE, we here propose that the robust Tr -Zr bonds and the flexibility of the bond angle in the $TrZr_8$ polyhedron is the origin of the anomalous anisotropic thermal expansion in $TrZr_2$.

At the end, we discuss future prospects on the observed anomalous thermal expansion in $TrZr_2$. Since the a -axis and the c -axis of $TrZr_2$ show contrasting thermal expansion (PTE and NTE), one of the expected applications is ZTE by tuning the changes in both axes. As a fact, the examined samples exhibit small expansion of the volume by cooling. The volume compression rate calculated by $[V(293\text{ K}) - V(50\text{ K})]/V(293\text{ K})$ for $CoZr_2$, $(Fe,Co,Ni)Zr_2$, and $(Fe,Co,Ni,Rh,Ir)Zr_2$ is -0.55%, -0.46%, and -0.11%, respectively. The trend suggests that alloying the Tr site by the HEA concept would be useful for achieving ZTE in $TrZr_2$. Furthermore, tunable volume thermal expansion is also a manufacturing advantage in the field of superconductivity application.^{22–24)} Another future prospect is the enhancement of T_c in $TrZr_2$. As discussed in Ref. 29, a larger lattice constant c is preferable for a higher T_c in $TrZr_2$. Therefore, if we could clarify the origin of the NTE of the c -axis in $TrZr_2$, a new superconductor with a T_c exceeding 12 K, which is higher than the T_c of $RhZr_2$, would be designed. In addition, the crystal structure analyses under high pressure are desired to clarify the origin of the enhancement of T_c by pressure and the link to the anomalous thermal expansion in $TrZr_2$ reported here.

In conclusion, we have analyzed the crystal structure of the $CuAl_2$ -type transition-metal zirconides $CoZr_2$, $(Fe,Co,Ni)Zr_2$, and $(Fe,Co,Ni,Rh,Ir)Zr_2$ using neutron powder diffraction at low temperatures and X-ray powder diffraction at high temperatures. With decreasing temperature, all samples showed a -axis shrinkage (PTE) and c -axis expansion (NTE). The anomalous (contrasting and anisotropic) thermal expansion of the a -axis and the c -axis in $TrZr_2$ is explained by the small change in the Tr -Zr distance and the systematic decrease in the Zr - Tr - Zr angle, which results in elongation of the unit cell along the c -axis. Although the origin of the structural change is still unclear, we consider that the flexible bonding of the $TrZr_8$ polyhedron units is essential for the NTE of the c -axis in $TrZr_2$.

Acknowledgments

The authors would like to thank M. Fujita and O. Miura for their supports in experiments and discussion. This work was performed under the GIMRT Program of the Institute for Materials Research, Tohoku University (CN: Center of Neutron Science for Advanced Materials: Proposal No. 202112-CNKXX-0001). This work was carried out by the JRR-3 program managed by the Institute for Solid State Physics, the University of Tokyo (the T1-3 HERMES IRT program: Proposal No. 22410). This work was partly supported by Grant-in-Aid for Scientific Research (KAKENHI) (Proposal Nos. 21K18834, 21H00151, 19H05164, and 21H00139) and Tokyo Government Advanced Research (H31-1).

References

- 1) K. Takenaka, *Sci. Technol. Adv. Mater.* 13, 013001 (2012).
- 2) G. D. Barrera, J. A. O. Bruno, T. H. K. Barron, and N. L. Allan, *J. Phys.: Condens. Matter* 17, R217 (2005).
- 3) J. Chen, L. Hu, J. Deng, and X. Xing, *Chem. Soc. Rev.* 44, 3522 (2015).
- 4) T. A. Mary, J. S. O. Evans, T. Vogt, and A. W. Sleight, *Science* 272, 90 (1996).
- 5) K. Takenaka, Y. Okamoto, T. Shinoda, N. Katayama, and Y. Sakai, *Nat. Commun.* 8, 14102 (2016).
- 6) M. Braden, G. André, S. Nakatsuji, and Y. Maeno, *Phys. Rev. B* 58, 847 (1998).
- 7) R. Huang, Y. Liu, W. Fan, J. Tan, F. Xiao, L. Qian, and L. Li, *J. Am. Chem. Soc.* 135, 11469 (2013).
- 8) Y. Y. Zhao, F. X. Hu, L. F. Bao, J. Wang, H. Wu, Q. Z. Huang, R. R. Wu, Y. Liu, F. R. Shen, H. Kuang, M. Zhang, W. L. Zuo, X. Q. Zheng, J. R. Sun, and B. G. Shen, *J. Am. Chem. Soc.* 137, 1746 (2015).
- 9) I. Yamada, K. Tsuchida, K. Ohgushi, N. Hayashi, J. Kim, N. Tsuji, R. Takahashi, M. Matsushita, N. Nishiyama, T. Inoue, T. Irifune, K. Kato, M. Takata, and M. Takano, *Angew. Chem. Int. Ed.* 50, 6579 (2011).
- 10) M. Azuma, W. Chen, H. Seki, M. Czapski, S. Olga, K. Oka, M. Mizumaki, T. Watanuki, N. Ishimatsu, N. Kawamura, S. Ishiwata, M. G. Tucker, Y. Shimakawa, J. P. Attfield, *Nat. Commun.* 2, 347 (2011).
- 11) J. R. Salvador, F. Guo, T. Hogan, M. G. Kanatzidis, *Nature* 425, 702 (2003).
- 12) T. Yokoyama and K. Eguchi, *Phys. Rev. Lett.* 107, 065901 (2011).
- 13) J. Chen, X. R. Xing, G. R. Liu, J. H. Li, and Y. T. Liu, *Appl. Phys. Lett.* 89, 101914 (2006).

- 14) X. R. Xing, J. X. Deng, J. Chen, and G. R. Liu, *Rare Metals* 22, 294 (2003).
- 15) S. L. Bud'ko, N. Ni, S. Nandi, G. M. Schmiedeshoff, and P. C. Canfield, *Phys. Rev. B* 79, 054525 (2009).
- 16) S. A. J. Kimber, D. N. Argyriou, F. Yokaichiya, K. Habicht, S. Gerischer, T. Hansen, T. Chatterji, R. Klingeler, C. Hess, G. Behr, A. Kondrat, and B. Büchner, *Phys. Rev. B* 78, 140503 (2008).
- 17) S. V. Pryanichnikov, S. G. Titova, G. A. Kalyuzhnaya, Yu. I. Gorina, and P. A. Slepukhin, *J. Exp. Theor. Phys.* 107, 69 (2008).
- 18) H. Fujishita, Y. Hayashi, M. Saito, H. Unno, H. Kaneko, H. Okamoto, M. Ohashi, Y. Kobayashi, and M. Sato, *Eur. Phys. J. B* 85, 52 (2012).
- 19) M. S. da Luz, J. J. Neumeier, R. K. Bollinger, A. S. Sefat, M. A. McGuire, R. Jin, B. C. Sales, and D. Mandrus, *Phys. Rev. B*, 2009, 79, 214505.
- 20) S. L. Bud'ko, N. Ni, and P. C. Canfield, *Philos. Mag.* 90, 1219 (2010).
- 21) J. J. Neumeier, T. Tomita, M. Debessai, J. S. Schilling, P. W. Barnes, D. G. Hinks, and J. D. Jorgensen, *Phys. Rev. B* 72, 220505 (2005).
- 22) A. F. Clark, G. Fujii, and M. A. Ranney, *IEEE Trans. Magn.* 17, 2316 (1981).
- 23) C. Xin, X. Wang, M. Guan, and Y. Zhou, *J. Supercond. Nov. Magn.* 28, 437 (2015).
- 24) A.V. Pogrebnyakov, J. M. Redwing, S. Raghavan, V. Vaithyanathan, D. G. Schlom, S.Y. Xu, Qi Li, D. A. Tenne, A. Soukiassian, X. X. Xi, M. D. Johannes, D. Kasinathan, W. E. Pickett, J. S. Wu, and J. C. H. Spence, *Phys. Rev. Lett.* 93, 147006 (2004).
- 25) Z. Fisk, R. Viswanathan, and G. W. Webb, *Solid State Commun.* 15, 1799 (1974).
- 26) A. Teruya, M. Kakihana, T. Takeuchi, D. Aoki, F. Honda, A. Nakamura, Y. Haga, K. Matsubayashi, Y. Uwatoko, H. Harima, M. Hedo, T. Nakama, and Y. Ōnuki, *J. Phys. Soc. Jpn.* 85, 034706 (2016).
- 27) Y. Mizuguchi and A. Yamashita, *Intechopen* (online book chapter), DOI: 10.5772/intechopen.96156.
- 28) Y. Mizuguchi, Md. R. Kasem, and T. D. Matsuda, *Mater. Res. Lett.* 9, 141 (2021).
- 29) Md. R. Kasem, A. Yamashita, Y. Goto, T. D. Matsuda, Y. Mizuguchi, *J. Mater. Sci.* 56, 9499 (2021).
- 30) K. Ohoyama, T. Kanouchi, K. Nemoto, M. Ohashi, T. Kajitani, and Y. Yamaguchi, *Jpn. J. App. Phys.* 37, 3319 (1998).
- 31) Y. Nambu et al., under preparation.
- 32) F. Izumi and K. Momma, *Solid State Phenom.* 130, 15 (2007).
- 33) K. Momma and F. Izumi, *J. Appl. Crystallogr.* 44, 1272 (2011).

Figure Captions

Fig.1. Schematic images of the crystal structure of CoZr_2 . The solid line in the lower figure shows the unit cell of CoZr_2 .

Fig. 2. (a) NPD patterns for CoZr_2 collected at $T = 50, 100, 170, 293$ K. (b) NPD patterns near the 200 and 002 peaks. (c) Rietveld refinement results for the NPD data for CoZr_2 ($T = 293$ K). The numbers indicate Miller indices. (d–f) Temperature dependence of lattice constant a , c , and V for CoZr_2 . NPD and XRD denote neutron powder diffraction and X-ray powder diffraction, respectively.

Fig. 3. Low-temperature lattice constants determined from neutron powder diffraction for alloyed TrZr_2 . (a–c) Temperature dependence of lattice constant a , c , and V for $\text{Fe}_{1/3}\text{Co}_{1/3}\text{Ni}_{1/3}\text{Zr}_2$. (d–f) Temperature dependence of lattice constant a , c , and V for $\text{Fe}_{0.2}\text{Co}_{0.2}\text{Ni}_{0.2}\text{Rh}_{0.2}\text{Ir}_{0.2}\text{Zr}_2$.

Table I. Structural parameters of CoZr_2 obtained from the Rietveld refinement. The atomic coordinates for the Zr and Co site are $(x, x+0.5, 0)$ and $(0, 0, 0.25)$, respectively.

	$T = 293$ K	$T = 170$ K	$T = 100$ K	$T = 50$ K
Space group	$I4/mcm$ (#140)			
Lattice constant a (Å)	6.3584(3)	6.3409(3)	6.3337(3)	6.3287(3)
Lattice constant c (Å)	5.5002(3)	5.5074(3)	5.5159(2)	5.5217(2)
V (Å ³)	222.37(2)	221.44(2)	221.28(2)	221.16(2)
R_{wp} (%)	16.41	16.02	14.31	13.84
S	1.46	1.64	1.54	1.50
x (Zr)	0.1710(2)	0.1720(2)	0.1717(2)	0.1715(2)
U_{iso} for Zr (Å ²)	0.0258(13)	0.0139(11)	0.0106(9)	0.0088(9)
Co-Zr distance (Å)	2.7293(12)	2.7223(12)	2.7218(11)	2.7214(11)
Co-Co distance (i) (Å)	2.7501(2)	2.7537(2)	2.75795(11)	2.76085(11)
Co-Co distance (ii) (Å)	4.4961(3)	4.4837(3)	4.4786(3)	4.4751(3)
Zr-Zr distance (i) (Å)	3.0954(12)	3.0887(12)	3.0942(12)	3.0979(12)
Zr-Zr distance (ii) (Å)	3.334(2)	3.321(2)	3.319(2)	3.317(2)
Zr-Co-Zr angle (deg.)	119.49(3)	119.24(3)	119.12(3)	119.04(3)

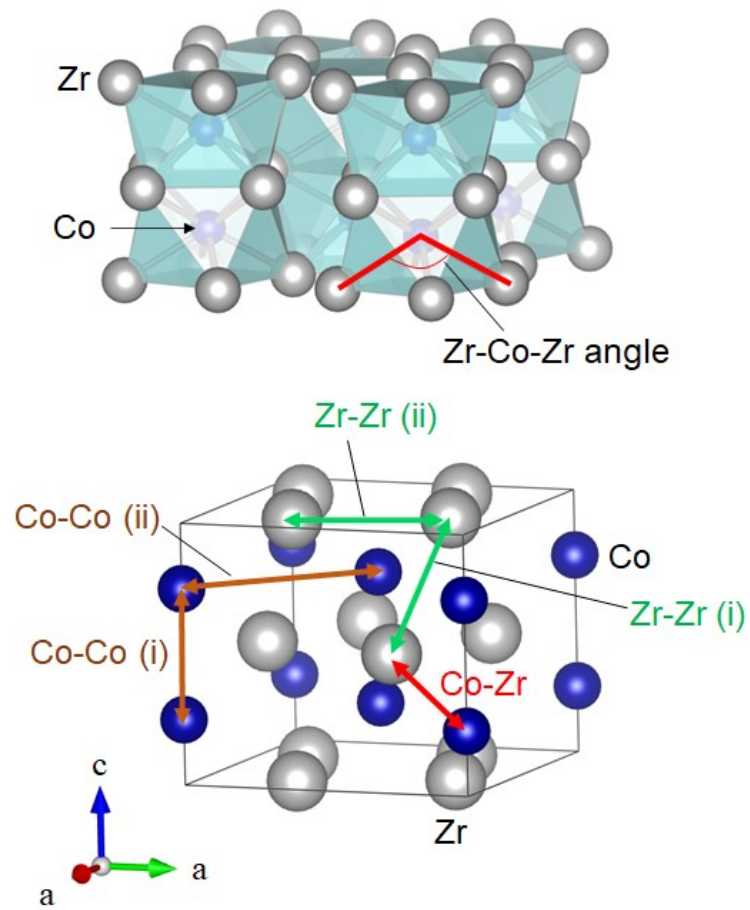


Fig.1. Schematic images of the crystal structure of CoZr_2 . The solid line in the lower figure shows the unit cell of CoZr_2 .

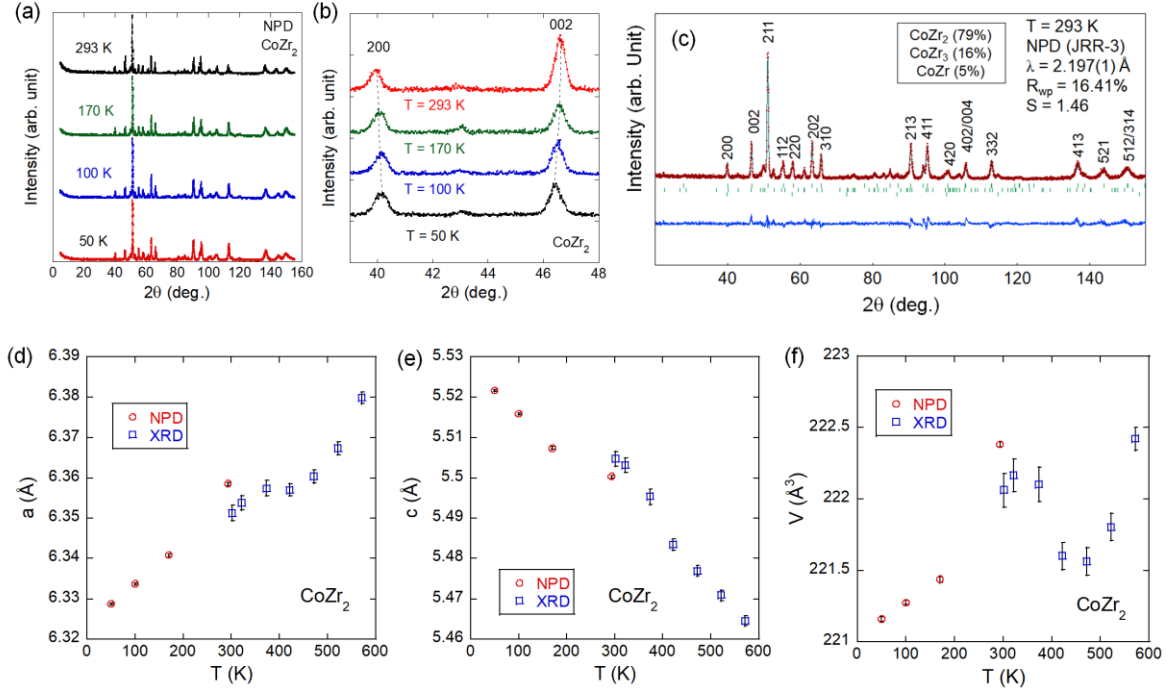


Fig. 2. (a) NPD patterns for CoZr_2 collected at $T = 50, 100, 170, 293$ K. (b) NPD patterns near the 200 and 002 peaks. (c) Rietveld refinement results for the NPD data for CoZr_2 ($T = 293$ K). The numbers indicate Miller indices. (d–f) Temperature dependence of lattice constant a , c , and V for CoZr_2 . NPD and XRD denote neutron powder diffraction and X-ray powder diffraction, respectively.

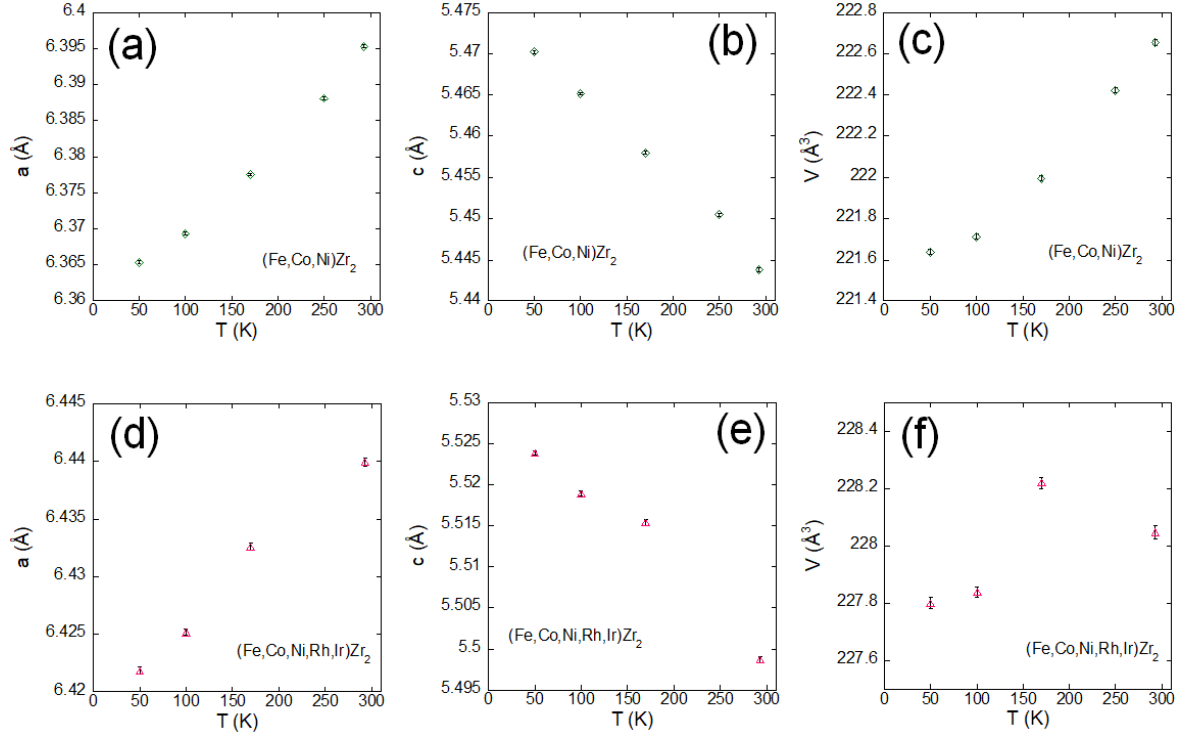


Fig. 3. Low-temperature lattice constants determined from neutron powder diffraction for alloyed TrZr_2 . (a–c) Temperature dependence of lattice constant a , c , and V for $\text{Fe}_{1/3}\text{Co}_{1/3}\text{Ni}_{1/3}\text{Zr}_2$. (d–f) Temperature dependence of lattice constant a , c , and V for $\text{Fe}_{0.2}\text{Co}_{0.2}\text{Ni}_{0.2}\text{Rh}_{0.2}\text{Ir}_{0.2}\text{Zr}_2$.

Supplementary data

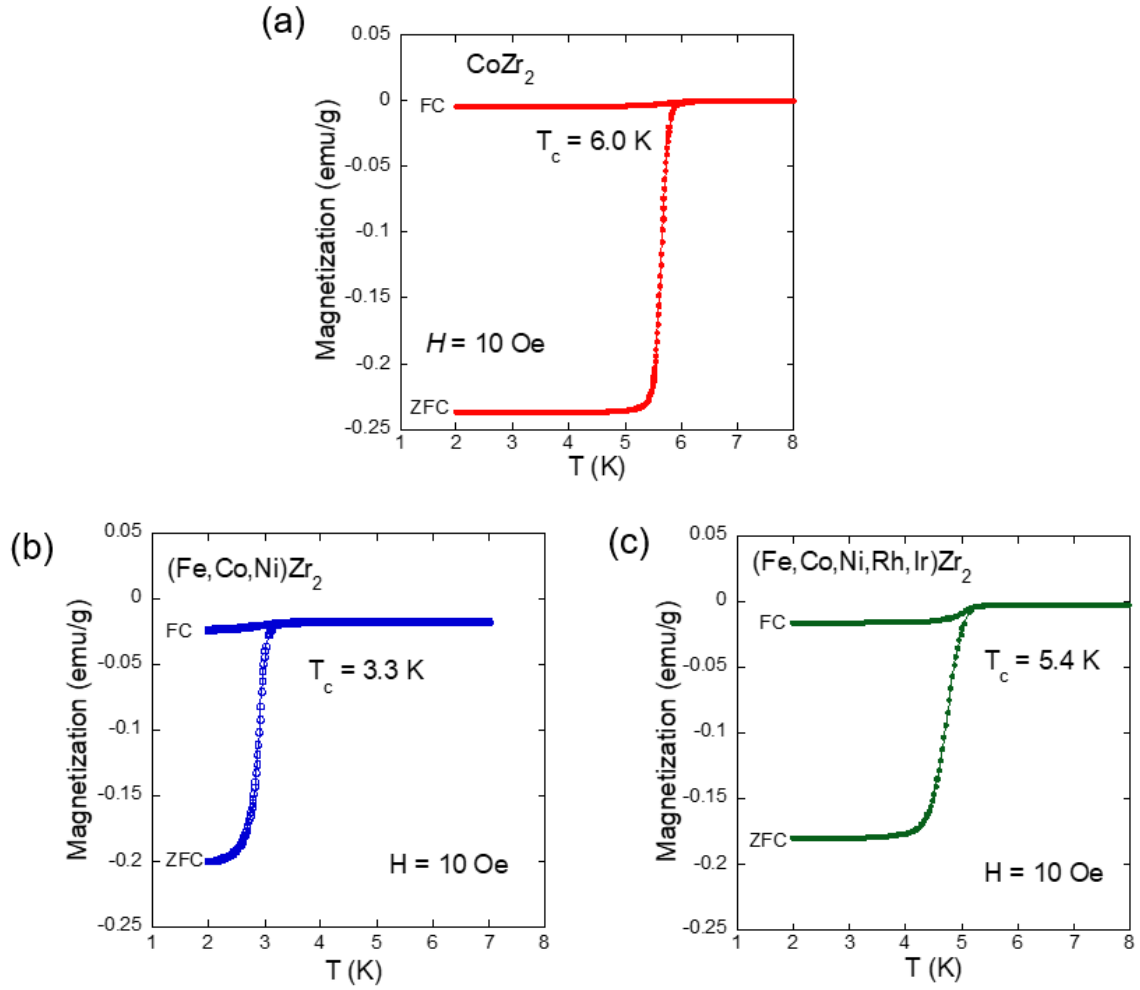


Fig. S1. Temperature dependence of magnetization after zero-field cooling (ZFC) and field cooling (FC) for TrZr_2 samples used in this study.

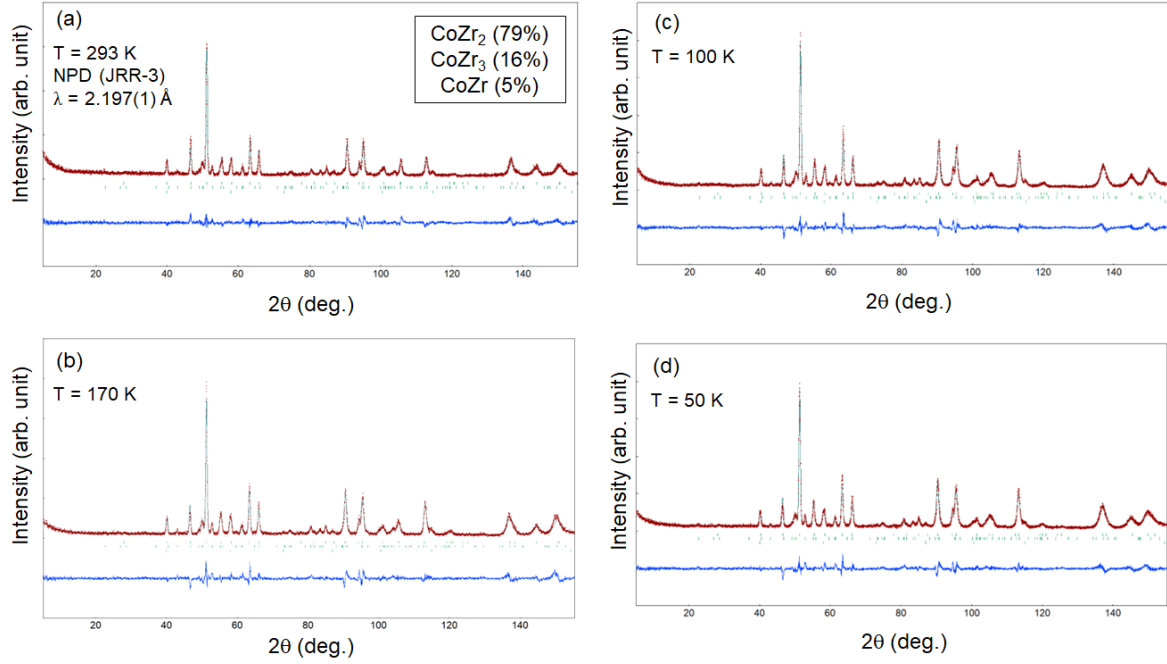


Fig. S2. Rietveld refinement results for NPD data for CoZr_2 collected at (a) 293 K, (b) 170 K, (c) 100 K, and (d) 50 K.

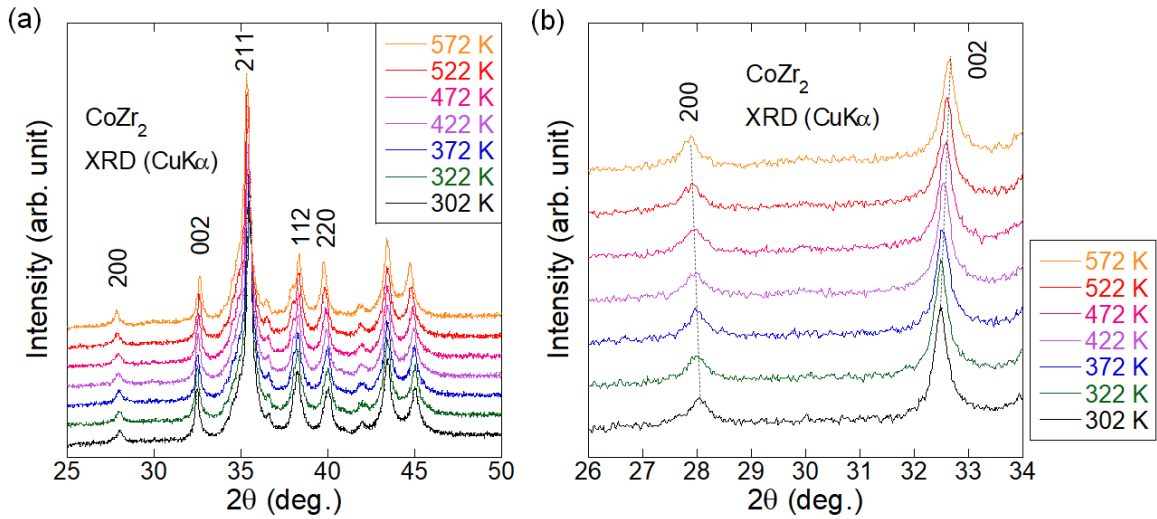


Fig. S3. (a) High-temperature powder XRD patterns for CoZr_2 . (b) XRD profiles near 200 and 002 peaks. The numbers indicate Miller indices.

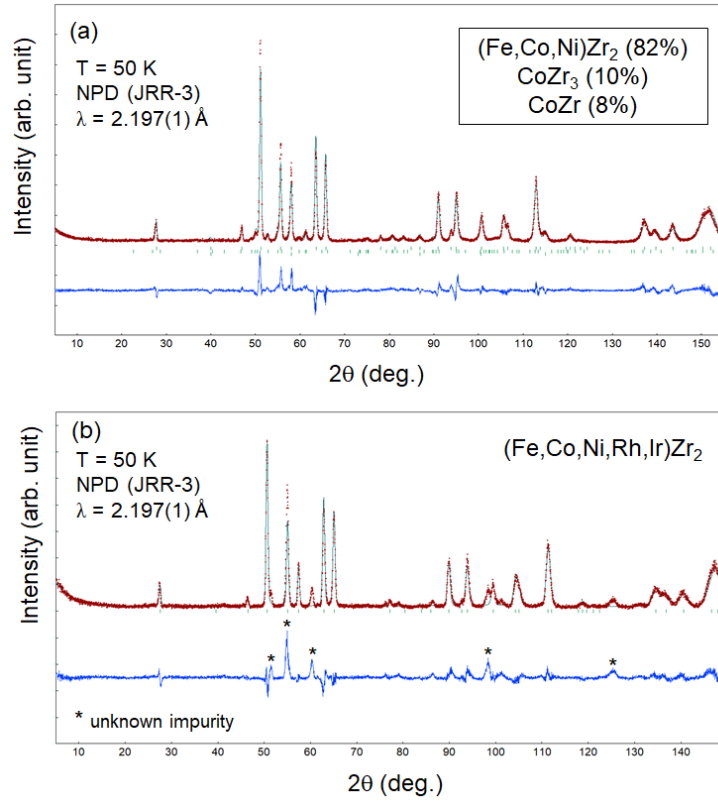


Fig. S4. Rietveld refinement results for NPD data collected at 50 K on (a) $\text{Fe}_{1/3}\text{Co}_{1/3}\text{Ni}_{1/3}\text{Zr}_2$ and (b) $\text{Fe}_{0.2}\text{Co}_{0.2}\text{Ni}_{0.2}\text{Rh}_{0.2}\text{Ir}_{0.2}\text{Zr}_2$. For $\text{Fe}_{1/3}\text{Co}_{1/3}\text{Ni}_{1/3}\text{Zr}_2$, three-phase refinement was performed, and single-phase refinement was applied for $\text{Fe}_{0.2}\text{Co}_{0.2}\text{Ni}_{0.2}\text{Rh}_{0.2}\text{Ir}_{0.2}\text{Zr}_2$.

Table S1. Structural parameters of (Fe,Co,Ni)Zr₂ obtained from the Rietveld refinement. The atomic coordinates for the Zr and *Tr* site are (*x*, *x*+0.5, 0) and (0, 0, 0.25), respectively.

	<i>T</i> = 293 K	<i>T</i> = 250 K	<i>T</i> = 170 K	<i>T</i> = 100 K	<i>T</i> = 50 K
<i>a</i> (Å)	6.3953(2)	6.3881(2)	6.3775(2)	6.3694(2)	6.3653(2)
<i>c</i> (Å)	5.4438(2)	5.4505(2)	5.4580(2)	5.4651(2)	5.4702(2)
<i>V</i> (Å ³)	222.655(14)	222.423(12)	221.994(11)	221.713(12)	221.639(12)
<i>R</i> _{wp} (%)	20.7	18.1	16.1	15.9	16.3
<i>S</i>	2.2	2.3	2.0	2.1	2.1
<i>x</i> (Zr)	0.1693(3)	0.1690(2)	0.1685(2)	0.1692(2)	0.1701(2)
<i>U</i> _{iso} for Zr (Å ²)	0.0342(9)	0.0211(8)	0.0174(7)	0.0167(7)	0.0178(7)
<i>Tr</i> -Zr (Å)	2.738(2)	2.7374(12)	2.7361(12)	2.7327(12)	2.7299(12)
<i>Tr</i> - <i>Tr</i> (i) (Å)	2.72190(11)	2.72525(11)	2.72900(11)	2.73255(11)	2.73510(11)
<i>Tr</i> - <i>Tr</i> (ii) (Å)	4.5222(2)	4.5171(2)	4.5096(2)	4.5039(2)	4.5010(2)
Zr-Zr (i) (Å)	3.089(2)	3.0934(13)	3.0998(13)	3.0961(13)	3.0903(12)
Zr-Zr (ii) (Å)	3.360(3)	3.358(2)	3.354(2)	3.347(2)	3.341(2)
Zr- <i>Tr</i> -Zr angle (deg.)	120.39(4)	120.29(3)	120.17(3)	120.00(3)	119.87(3)

Table S2. Structural parameters of (Fe,Co,Ni,Rh,Ir)Zr₂ obtained from the Rietveld refinement. The atomic coordinates for the Zr and *Tr* site are (*x*, *x*+0.5, 0) and (0, 0, 0.25), respectively.

	<i>T</i> = 293 K	<i>T</i> = 250 K	<i>T</i> = 100 K	<i>T</i> = 50 K
<i>a</i> (Å)	6.4400(3)	6.4326(3)	6.4252(3)	6.4218(3)
<i>c</i> (Å)	5.4987(4)	5.5154(3)	5.5190(3)	5.5239(3)
<i>V</i> (Å ³)	228.05(2)	228.22(2)	227.83(2)	227.80(2)
<i>R</i> _{wp} (%)	23.5	22.6	20.6	21.4
<i>S</i>	1.7	2.0	1.9	2.0
<i>x</i> (Zr)	0.1673(3)	0.1694(3)	0.1693(2)	0.1687(2)
<i>U</i> _{iso} for Zr (Å ²)	0.0277(12)	0.0188(10)	0.0185(9)	0.0193(9)
<i>Tr</i> -Zr (Å)	2.764(2)	2.759(2)	2.7571(12)	2.7581(12)
<i>Tr</i> - <i>Tr</i> (i) (Å)	2.7494(3)	2.7577(2)	2.7595(2)	2.7620(2)
<i>Tr</i> - <i>Tr</i> (ii) (Å)	4.5537(3)	4.5485(3)	4.5433(3)	4.5409(3)
Zr-Zr (i) (Å)	3.135(2)	3.123(2)	3.1250(13)	3.1319(13)
Zr-Zr (ii) (Å)	3.392(3)	3.379(3)	3.376(2)	3.376(2)
Zr- <i>Tr</i> -Zr angle (deg.)	120.36(5)	120.03(5)	119.94(3)	119.91(3)